Excitons in metal halide perovskite nanoplatelets: an effective mass description of polaronic, dielectric and quantum confinement effects†

Jose L. Movilla, [ID] [a] Josep Planelles [ID] [b] and Juan I. Climente [ID] *[b]

A theoretical model for excitons confined in metal halide perovskite nanoplatelets is presented. The model accounts for quantum confinement, dielectric confinement, short and long range polaron interactions by means of effective mass theory, image charges and Haken potentials. We use it to describe the band edge exciton of $MAPbI_3$ structures surrounded by organic ligands. It is shown that the quasi-2D quantum and dielectric confinement squeezes the exciton radius, and this in turn enhances short-range polaron effects as compared to 3D structures. Dielectric screening is then weaker than expected from the static dielectric constant. This boosts the binding energies and radiative recombination probabilities, which is a requisite to match experimental data in related systems. The thickness dependence of Coulomb polarization and self-energy potentials is in fair agreement with sophisticated atomistic models.

1 Introduction

In the last years, 2D layered hybrid (organic–inorganic) metal halide perovskites and nanoplatelets (NPLs) have emerged as a new class of quasi-two-dimensional materials with outstanding optical (photovoltaic, light-emitting) properties and improved moisture stability as compared to their 3D counterparts.[1–12] The optical properties of these objects are intimately connected with the electronic structure of the band edge exciton. A large number of experimental and theoretical studies have investigated how the exciton electronic structure changes with the thickness and composition of either the inorganic layers, and those of the organic ligands in between consecutive layers.[7,13–25] It is now clear that the electronic structure results from an interplay between the strong quantum confinement of the inorganic layers (the ligands have large gaps and hence act as potential barriers) and the strong dielectric confinement (the ligands have typically small dielectric constant).

While the separation between quantum and dielectric confinement effects is difficult by experimental means, computational simulations allow one to visualize the impact of each factor,[26] thus paving the way towards optimal engineering of optoelectronic devices based on these materials.[27] A similar scenario has been found in II–VI NPLs. Here, effective mass models have proved very useful in providing intuitive interpretations of a wide variety of experimental observations. These include exciton energy and oscillator strength dependence on the composition and material thickness,[28–32] exciton binding energies,[33–38] heterostructure details,[33,39–42] absorption and emission directionality[43] and non-linear optical properties.[44,45] It is naturally desirable to extend effective mass models to halide perovskite quasi-2D materials. Input parameters such as effective masses and dielectric constants can be inferred from atomistic simulations already present in the literature.[46] Initial studies have been already conducted in this direction.[24,47] However, there is a physical factor which has not been considered to date, and yet it constitutes a differential trait with respect to II–VI NPLs. Namely, the presence of sizable polaron effects, with distinct short-range and long-range response.[48]

Polaron effects entail non-negligible carrier-phonon coupling. These are significant in hybrid metal halide perovskites because of the softness of the lattice,[49] the low phonon energies[50–52] and the high difference between static and high-frequency dielectric constants in these materials.[51,53–55] All these factors lead to Frölich constants (exciton-LO phonon coupling) up to one order of magnitude greater than in II–VI materials.[48] There has been increasing awareness of the importance of polaron effects not only in 3D bulk hybrid perovskites,[56–59] but also in 2D layered ones. They have been shown to increase exciton effective masses,[48] affect their spin dynamics,[60,61] radiative recombination,[62] binding energy[63] and even lead to self-trapping.[64]

The softness of the lattice implies large polaron radii (∼1 nm). Outside the polaron, the electrical charge is strongly

[a]*Departament d'Educació i Didàctiques Específiques, Universitat Jaume I, Av. Sos Baynat, s/n, 12071 Castelló, Spain*

[b]*Departament de Química Física i Analítica, Universitat Jaume I, Av. Sos Baynat, s/n, 12071 Castelló, Spain. E-mail: climente@uji.es*

† Electronic supplementary information (ESI) available: Mathematica code to calculate the exciton binding energy, radius and oscillator strength using our model (with either Haken or Bajaj polaron potential). See DOI: https://doi.org/10.1039/d3na00592e

screened by its phonon cloud. Inside it, however, the screening is much weaker. The distance dependence of the charge screening is a relevant factor in the description of excitons, since electron and hole polarons are attracted and hence tend to couple.[48]

Because direct inclusion of polaron effects in exciton calculations is a major challenge, semi-empirical approximations have been proposed in the literature. One such case is the Haken potential.[65] By including the electron and hole polaron radii – which can be inferred from experiments and atomistic calculations[51,64] – as a parameter, the electron–hole Coulomb potential is rewritten as:

$$V(r) = -\frac{1}{\varepsilon_s}\frac{q^2}{r} - \frac{1}{\varepsilon^*}\frac{q^2}{r}\frac{e^{-r/l_e} + e^{-r/l_h}}{2} = V_C + V_Y. \qquad (1)$$

The above expression, which is explained in more detail in the next section, contains a first term (V_C) describing the standard Coulomb interaction (with full, static screening) plus a second term (V_Y) which introduces the ionic screening correction at short distances. The latter mimics the inability of the lattice to screen the interaction when the electron–hole pair is very close (below the polaron radius), thus enhancing excitonic interactions. The Haken potential (and similar potentials, such as the Bajaj[66] and Pollman–Büttner[67] ones) have been shown to improve the estimates of the exciton binding energy in 3D metal halide perovskites as compared to estimates considering bare Coulomb potentials, reconciling some controversial observations in experiments.[48,59]

The goal of this article is to extend the effective mass theory description of excitons in quasi-2D systems, previously developed for II–VI NPLs,[33] for the case of hybrid metal halide perovskites. This is done by considering not only quantum and dielectric confinement, but also short- and long-range polaron screening – through the inclusion of Haken-like potentials – the technical novelty lies in the conjugation of dielectric confinement and polaronic effects. The former is conveniently expressed using the image charge method for quantum well-like structures,[68] which has proved valuable in the description of II–VI NPLs with varying thickness.[31,33,34,36,42] Such a method was however posed for Coulomb-law potentials, V_C. Here we adapt it to account for the additional Yukawa-like potential present in eqn (1), V_Y.

We derive image charge expressions for both electron–hole interaction and for the self-energy corrections. The latter result from the interactions of carriers with their own image charges. Self-energy terms, which escape from simple Keldysh potentials often used to model dielectric confinement,[21,37] are particularly important for accurate estimates of the excitonic band gap[42,46] or exciton interactions across the organic barrier separating inorganic layers.[69]

Our model is tested for the prototypical case of MAPbI$_3$. We find remarkable agreement with the self-energy obtained from *ab initio* calculations[23] for NPLs down to a single layer, by including a single phenomenological parameter related to the non-abrupt profile of the dielectric constant in the vicinity of the organic–inorganic interfaces. We also show that polaronic

interactions have a prominent role in excitons confined in few-layers metal halide perovskites. This is because the strong quantum and dielectric confinement squeeze the exciton under the polaron radius. It is then possible to explain the large binding energies reported in experiments.

2 Theoretical framework

Within the effective mass formalism, the exciton ground state of a quasi-2D structure subject to quantum and dielectric confinement can be obtained from:[33]

$$H = \sum_{i=e,h}\left(\frac{\mathbf{p}_i^2}{2m_i} + V_i^{self} + V_i^{pot}\right) + V_{eh} + E_{gap}{}^\Gamma, \qquad (2)$$

where e and h indexes stand for electron and hole, $\mathbf{p}_i$ for the momentum operator, m_i for the effective mass of carrier i and $E_{gap}{}^\Gamma$ for the energy gap between the conduction and the valence band at the Γ point. V_i^{pot} is the confining potential set by the band offset between the perovskite layers and the surrounding ligands. Because the organic character of such ligands prevents carriers from tunneling,[19,21] it is convenient to set $V_i^{pot} = 0$ inside the perovskite domain and $V_i^{pot} = \infty$ outside. V_i^{self} and V_{eh} are the self-energy and electron–hole Coulomb potentials, which can be calculated using the image-charge method for quantum wells[68] to account for dielectric mismatch effects.

Eqn (2) has been employed on different occasions to study excitons in II–VI NPLs.[33,34,38,42] Its extension to hybrid halide perovskite materials, requires including interparticle distance dependent polaron coupling. This can be done by modifying V_i^{self} and V_{eh} with respect to their usual expressions. Below we describe the procedure to do so.

Neglecting for the time being dielectric mismatch, polaron coupling effects are efficiently described by the Haken potential, which in a.u. reads:[65]

$$\begin{aligned}V_{eh}^{bulk}(r) &= -\frac{q^2}{\varepsilon_\infty r} + \frac{q^2}{r}\left(\frac{1}{\varepsilon_\infty} - \frac{1}{\varepsilon_s}\right)\left[1 - \frac{e^{-\beta_e r} + e^{-\beta_h r}}{2}\right]\\ &= -\frac{q^2}{\varepsilon_s r} - \frac{q^2}{\varepsilon^* r}\frac{e^{-\beta_e r} + e^{-\beta_h r}}{2}.\end{aligned} \qquad (3)$$

Here, r is the electron–hole distance, q the fundamental charge, ε_s the static dielectric constant and ε_∞ the high frequency (optical) one. The term $\left(\frac{1}{\varepsilon_\infty} - \frac{1}{\varepsilon_s}\right) = \frac{1}{\varepsilon^*}$ represents ionic screening of carriers. β_i are the electron and hole polaron radii inverse: $\beta_i = l_i^{-1} = (2m_i\omega_{LO}/\hbar)^{1/2}$, with $\hbar\omega_{LO}$ the longitudinal optical phonon frequency.

Eqn (3) can be viewed either as an increase of the electron–hole interaction by the reduction of the ionic screening of carriers at short distances (first line) or as if charges embedded in polar semiconductors had a two-fold interaction: a standard screened Coulomb (long range) interaction supplemented by a Yukawa-like (short range) interaction in a medium of effective dielectric constant ε^* ($V_{eh} = V_C + V_Y$, second line in the equation). We adopt the second point of view in this work.

To include dielectric mismatch in V_{eh}, we rely on the image charge method. Usual expressions found in the literature are

obtained from Coulomb interaction terms (V_C).[68,70] Here we need to revisit their derivation for the Yukawa-like terms (V_Y). The Yukawa potential is not solution of the Poisson equation, that accounts for the electromagnetic interactions carried by massless photons, and that for a point source charge in vacuum reads (MKS units):

$$\nabla^2 \Psi_C = -\frac{q}{\varepsilon_0} \delta(\mathbf{r}), \qquad (4)$$

with ε_0 the vacuum permittivity and Ψ_C the electrostatic potential. Rather, the carriers of the Yukawa interactions have finite mass. Then, the Poisson equation should be modified by including a mass (μ) term as follows:[71]

$$\nabla^2 \Psi_Y - \mu^2 \Psi_Y = -\frac{q}{\varepsilon_0} \delta(\mathbf{r}), \qquad (5)$$

The integration of eqn (5) yields back the Yukawa potential:

$$\Psi_Y(r) = \frac{q}{4\pi\varepsilon_0} \frac{e^{-\mu r}}{r}. \qquad (6)$$

In a dielectric medium other than the vacuum we should replace ε_0 by a dielectric constant ε_1, and for a given charge distribution ρ we should replace $q\delta(\mathbf{r})$ by ρ. All and all, eqn (5) reads:

$$\varepsilon_1 \nabla^2 \Psi_Y - \varepsilon_1 \mu^2 \Psi_Y = -\rho \qquad (7)$$

In order to determine the interface boundary conditions between two homogeneous materials with different dielectric constant, and taking into account the definition of the electric displacement vector $\mathbf{D} = -\varepsilon\nabla\Psi_Y$, we can rewrite eqn (7) as $\nabla\cdot\mathbf{D} = \rho - \mu'^2\Psi_Y$, with $\mu' = \sqrt{\varepsilon}\mu$. Then, we consider a thin, dz height slab around the interface and integrate this equation,

$$\int \nabla\cdot\mathbf{D}\,dV = \int \rho\,dV - \mu'^2 \int \Psi_Y\,dV. \qquad (8)$$

By taking into account the continuity of Ψ_Y across the boundary, we see that as $dz \to 0$ the second integral approaches zero. If we additionally use the divergence theorem to transform volumetric integrals into surface ones, we find:

$$\int (\mathbf{D}_1 - \mathbf{D}_2)\cdot\mathbf{u}_z\,dA = \int \sigma\,dA \to \mathbf{D}_{1\perp} - \mathbf{D}_{2\perp} = \sigma, \qquad (9)$$

with $\mathbf{u}_z$ a unit vector crossing the interace, A the area of integration, and σ the electric charge density on the interface. The relevant result here is that the obtained boundary condition of Ψ_Y coincides with the usual one for Coulomb potentials, Ψ_C.

We can also show that the charge density generated by the Yukawa field on a dielectrically mismatched interface is similar to that of the Coulomb one. The potential

$$\Psi_Y(r) = \frac{1}{4\pi\varepsilon_0} \frac{1}{\varepsilon_1^*} \frac{q}{r} e^{-\beta r} \qquad (10)$$

yields an electric field, $\mathbf{E}_Y = -\nabla\Psi_Y$. Since ∇ in spherical coordinates reads

$$\nabla = \frac{\partial}{\partial r}\mathbf{u}_r + \frac{1}{r}\frac{\partial}{\partial\theta}\mathbf{u}_\theta + \frac{1}{r\sin\theta}\frac{\partial}{\partial\phi}\mathbf{u}_\phi, \qquad (11)$$

then,

$$\mathbf{E}_Y = -\frac{\partial\Psi_Y}{\partial r}\mathbf{u}_r$$
$$= -\frac{\partial\Psi_Y}{\partial r}\left(\cos\theta\,\mathbf{u}_z + \sin\theta\cos\phi\,\mathbf{u}_x + \sin\theta\sin\phi\,\mathbf{u}_y\right), \qquad (12)$$

and the z-component of the field is:

$$E_z = -\frac{\partial\Psi_Y}{\partial r}\cos\theta = \frac{q}{\varepsilon_1^*}\frac{(1+\beta r)e^{-\beta r}}{r^2}\cos\theta. \qquad (13)$$

The boundary conditions at the interface between this medium and a rigid (*i.e.*, non-polaronic) one defined by a static dielectric constant ε_2 are given by eqn (9). Then,

$$\varepsilon_1^*\left(E_z - \frac{\sigma}{2\varepsilon_0}\right) = \varepsilon_2\left(E_z + \frac{\sigma}{2\varepsilon_0}\right) \to \frac{\sigma}{\varepsilon_0} = 2E_z\frac{\varepsilon_1^* - \varepsilon_2}{\varepsilon_1^* + \varepsilon_2}. \qquad (14)$$

Using eqn (13) we get:

$$\sigma = \frac{1}{2\pi}\frac{q}{\varepsilon_1^*}\frac{\varepsilon_1^* - \varepsilon_2}{\varepsilon_1^* + \varepsilon_2}\frac{f(r)}{r^2}\cos\theta, \qquad (15)$$

with $f(r) = (1 + \beta r)e^{-\beta r}$. Note that this induced charge density is identical to that generated by a standard Coulomb potential in a rigid medium, but replacing $1/r^2$ by $f(r)/r^2$.

It should be noted that in the limit of zero polaron radius ($\beta \to \infty$), $(1 + \beta r)e^{-\beta r} = 0$. Then, the Yukawa induced charge density is zero. In any other case, we can replace the effect that this induced charge produces by the effect of an image charge q_i (located either in the position of the original charge or in its mirror position, *i.e.*, always located in the opposite region to that on which it acts) of magnitude

$$q_i = \frac{q}{\varepsilon_1^*}\frac{\varepsilon_1^* - \varepsilon_2}{\varepsilon_1^* + \varepsilon_2}, \qquad (16)$$

which generates a Yukawa potential $q_i e^{-\beta r}/(4\pi\varepsilon_0 r)$ instead of a Coulomb $q_i/(4\pi\varepsilon_0 r)$ one.

In summary, except that $1/r^2$ must be multiplied by a $f(r)$ term, the image charges are calculated as in standard rigid media. Consequently, the potential between electrons and holes in layered metal halide perovskites (considering dielectric confinement with interparticle distance-dependent polaronic contributions) can be obtained by slightly modifying the expressions provided in ref. 68 for rigid semiconductor quantum well-like structures. The modified potential reads as follows (back in a.u.):

$$V_{eh} = -\sum_{k=C,Y}\sum_{n=-\infty}^{\infty}\frac{q^2 q_{n,k} f_{n,k}(\mathbf{r}_e, \mathbf{r}_h)}{r_n}. \qquad (17)$$

Here,

$$r_n = \left\{\left(\mathbf{r}_{\|,e} - \mathbf{r}_{\|,h}\right)^2 + \left[z_e - (-1)^n z_h + nL_z\right]^2\right\}^{1/2}, \qquad (18)$$

with L_z the thickness of the perovskite layers, and

$$q_{n,k} = \frac{1}{\varepsilon_k}\left[\frac{\varepsilon_k - \varepsilon_2}{\varepsilon_k - \varepsilon_2}\right]^{|n|}, \tag{19}$$

with $\varepsilon_C = \varepsilon_s$ (the static dielectric constant of the perovskite material), $\varepsilon_Y = \varepsilon^*$ (ionic correction of the perovskite), and ε_2 the dielectric constant of the organic ligands. The functions $f_{n,k}$ are given by:

$$f_{n,C}(\mathbf{r}_e, \mathbf{r}_h) = 1, \tag{20}$$

$$f_{n,Y}(\mathbf{r}_e, \mathbf{r}_h) = \frac{1}{2}\left(e^{-\beta_e r_n} + e^{-\beta_h r_n}\right). \tag{21}$$

The self-polarization potentials of electron and hole can be obtained from eqn (17) by setting $\mathbf{r}_e = \mathbf{r}_h$, eliminating the $n = 0$ terms (which represent the interaction of a charge carrier with itself), and dividing by 2 as corresponds to a self-energy:[70]

$$V_{i=e,h}^{self} = \sum_{k=C,Y}\sum_{n=\pm1,\pm2,\ldots}\frac{q^2 q_{n,k}g_{n,k}(z_i)}{2|z_i - (-1)^n z_i + nL_z|}, \tag{22}$$

where now

$$g_{n,C}(z_i) = 1, \tag{23}$$

$$g_{n,Y}(z_i) = e^{-\beta_i|z_i - (-1)^n z_i + nL_z|}. \tag{24}$$

Once eqn (22) and (17) are plugged into Hamiltonian (2), the exciton ground state is obtained by integrating it with a variational wavefunction of the form

$$\psi_X = N\Phi_e\Phi_h\, e^{-\frac{\sqrt{\left(\mathbf{r}_{\parallel,e} - \mathbf{r}_{\parallel,h}\right)^2}}{a_B^*}}, \tag{25}$$

where N is a normalization factor, while Φ_e and Φ_h are the electron and hole single particle states, which account for quantum confinement. The exponential term is an in-plane Slater correlation factor, which captures excitonic interactions. a_B^* is the effective Bohr radius, which is optimized variationally by following the computational scheme described in ref. 72 and 33, including the modified potentials V_{eh} and V_i^{self} to incorporate the Yukawa-type potentials. At this regard, and for the sake of computational feasibility in the calculation of V_{eh}, the exponential factor in the Yukawa potential is spanned as a sum of five Gaussian functions, including five linear and five non-linear fitting parameters, which are optimized from the starting set provided in ref. 73.

A Mathematica code to carry out the above described procedure is provided in the ESI† for free use. The code has minimal memory requirements and can be executed in ordinary computers, providing exciton total and binding energies (sub-meV converged), effective Bohr radius and electron–hole overlap integral.

3 Results and discussion

In this section, our model is used to investigate the connection between polaronic, dielectric confinement and quantum confinement effects in quasi-2D halide perovskite layers. For illustrative

purposes, we consider MAPbI$_3$ (MA = methylammonium). Effective parameters for this material have been proposed in the literature: dielectric constants $\varepsilon_{s1} = 22.0$ and $\varepsilon_{\infty 1} = 5.6$,[23] effective masses $m_e = 0.19$, $m_h = 0.22$,[74] and phonon frequency $\hbar\omega_{LO} = 16.5$ meV,[48] which yield polaron radii of $l_e = 1/\beta_e = 0.94$ nm and $l_h = 1/\beta_h = 1.01$ nm. Unless otherwise noted, the low polarizability of the organic environment is characterized by $\varepsilon_2 = 2$.[21]

Fig. 1(a) shows the different material domains of the system under study. The perovskite layers are modeled as a dielectric NPL sandwiched by organic barriers, with abrupt (step function) interfaces. The lateral dimensions of the NPL are fixed at 30×30 nm^2. That is in the weak confinement (quantum-well like) regime. The number of layers defining the NPL thickness, n_L, is a variable. Each layer is constituted by a single octahedron (unit cell) with lattice parameter $a_0 = 0.63$ nm,[49] which add up to give a NPL thickness of $L_z = n_L a_0$.

Prior to dealing with the numerical simulations for heterostructures, it is instructive to get a qualitative view on the Haken potential in bulk MAPbI$_3$, as it defines the basic mechanism of carrier-lattice coupling we aim to study. Fig. 1(b) shows the profile of V_{eh}^{bulk}, given by eqn (3), as a function of the electron–hole distance, in units of the electron polaron radius l_e (blue line). Coulomb (V_C, red line) and Yukawa (V_Y, green line) contributions are also included. As can be observed, the Yukawa term is negligible for e–h separations of the order of $4l_e$, where $V_{eh}^{bulk} \approx V_C$. However, at lower e–h distances both contributions become significant. Eventually, for $r \leq l_e$, V_Y becomes more

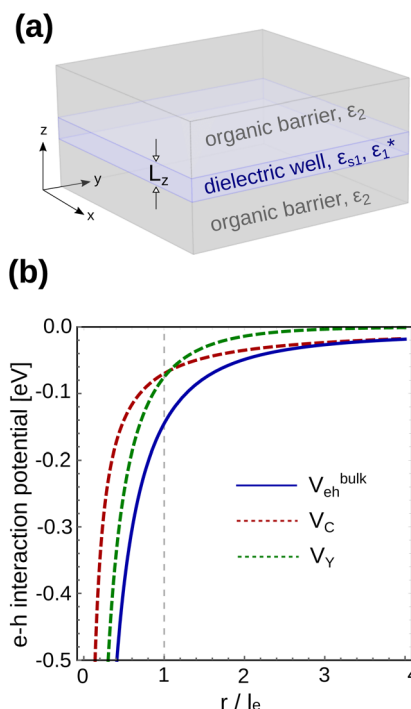**Fig. 1** (a) Schematic of the system under study. (b) Haken potential (blue, solid line) in bulk MAPbI$_3$ as a function of the electron–hole distance in units of the polaron radius l_e. Coulomb (V_C, red dashed line) and Yukawa (V_Y, green dashed line) contributions are also included. Note that these contributions invert their predominance at radii close to the polaron radius (highlighted by a vertical, dashed line).

important than V_C. In short, the smaller the exciton Bohr radius, the more relevant the Yukawa corrections. Major changes are expected when it approaches the polaron radius.

3.1 Exciton properties

We shall see next that quantum and dielectric confinement greatly reduce the exciton radius in layered perovskites with respect to their bulk value, and this indeed has a pronounced impact on its properties. Full dots in Fig. 2(a) represent the calculated exciton Bohr radius a_B^* (our variational parameter) as a function of the number of layers n_L conforming the NPL. For comparison, results excluding dielectric and polaron short range contributions are also shown in the figure (green triangles; ε_{s1} is assumed). It is clear from the trend of the triangles that the exciton radius diminishes with respect to its bulk value when the NPL becomes thinner. This is because the vertical quantum confinement reinforces exciton interactions in the plane.[33] Yet, the reduction is about 4 times greater in the presence of dielectric confinement and polaron short range interaction (full dots). The overall result is a surprisingly small exciton Bohr radius, which, for low enough n_L is comparable to that obtained by considering infinite polaron radii (open squares in the figure), *i.e.* as if $V_{eh} = -q^2/(\varepsilon_{\infty 1} r)$. In other words, in the few-layer limit the exciton becomes immune to the high ionic polarizability of metal halide perovskites.

Such small Bohr radii are expected to cause a sharp increase in the radiative recombination rates. The rate is proportional to the squared electron–hole overlap function, $S_{eh}^2 = |\langle \psi_X | \delta_{r=0} | 0 \rangle|^2$, which can be calculated analytically within our model.[33] Fig. 2(b) confirms the rapid increase of S_{eh}^2 with decreasing number of perovskite layers. This is consistent with the experimental observation of reduced photoluminescence lifetimes as the perovskite NPLs become thinner,[76] although a more direct comparison is hindered by the co-existence of non-radiative processes. Fig. 2(b) also shows that polaron short range effects raise S_{eh}^2 up to three times as compared to the case of static dielectric constant (*cf.* full dots and empty circles). This suggests that polaron coupling in NPLs enable faster radiative recombination than in more rigid semiconductors, such as metal chalcogenide ones.

Dielectric, polaron coupling and quantum confinement contributions also affect noticeably other exciton properties of interest, namely its binding energy E_b. This is shown in Fig. 2(c). Because the exciton Bohr radius in a strictly 2D system is half that of the 3D case, and $E_b = \hbar^2/2\mu a_B^{*2}$ (with μ the exciton reduced mass), the relationship $E_b^{2D} = 4E_b^{3D}$ has been often cited in the literature to summarize the effect of quantum confinement.[26,76] A close inspection to the green triangles in Fig. 2(c) confirms that E_b indeed increases as the perovskite becomes thinner by action of quantum confinement. However, the scale of the increase is greatly magnified upon inclusion of dielectric and polaron short range terms (full dots).

We can disentangle dielectric and polaronic coupling contributions in the analysis of E_b. The impact of dielectric confinement can be measured by the difference between green triangles and open circles in the figure. The former include only quantum confinement, while the latter add dielectric confinement but no polaron short range effects (static dielectric constant only). It is clear that dielectric confinement alone suffices to produce a large effect on E_b, from a 4-fold increase when $n_L = 8$ to a 14-fold increase when $n_L = 1$. This can be explained as a consequence of the large polarizability of metal halide perovskites. On the one hand, the large ε_{s1} constant of the perovskite makes the bare Coulomb contribution small. This justifies the small E_b values of the green triangles. On the other hand, the large $\varepsilon_{s1}/\varepsilon_2$ ratio implies a large dielectric contrast with the organic medium, which leads to enhanced surface polarization charges (or the image charges they project). These intensify the excitonic interaction, which results in much larger values of E_b for the empty circles.

The effect of polaron short range contributions can be visualized by comparing empty circles and full dots in Fig. 2(c). They become increasingly noticeable when the number of layers decreases, because a_B^* becomes comparable to the polaron radius (recall Fig. 2(a)). For $n_L = 1$, the enhancement exceeds a factor of 2 (*i.e.* 100% increase). It is worth noting too that even for thin NPLs, the actual E_b we calculate (full dots) have not reached the values expected in the limit of infinite polaron radius (squares). This means that relationships of the type $E_b^{2D} \propto (\varepsilon_{\infty 1}/\varepsilon_2)$, which are sometimes taken as reference in the literature,[26] provide an upper bound estimate.

Taken together, it is remarkable that the exciton binding energies are comparable or greater to those of II–VI semiconductor NPLs,[33–38] despite the large polarizability of
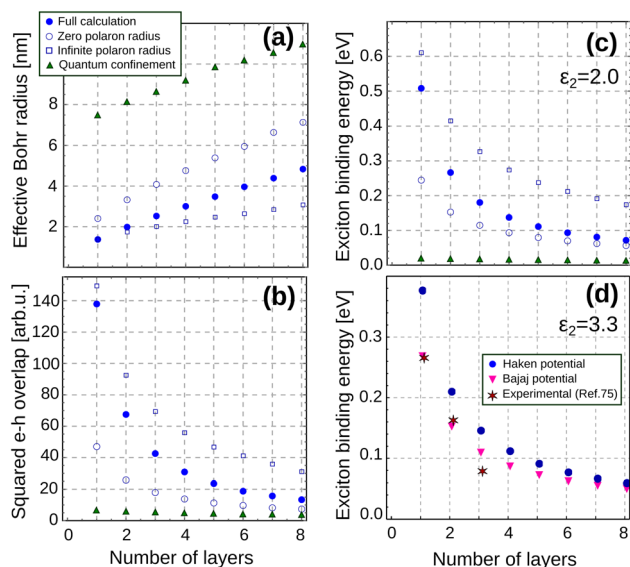

Fig. 2 Thickness dependence of exciton properties in MAPbI$_3$ layers. (a) Exciton effective Bohr radius. (b) Electron–hole overlap squared. (c) Exciton binding energy. The organic barriers have $\varepsilon_2 = 2$. Results are depicted for different degrees of approximation in the model. Blue dots: full calculation. Empty circles: zero polaron radius ($V_Y = 0$, $\varepsilon_{s1} = 22$). Squares: infinite polaron radius ($V_Y = 0$, $\varepsilon_{s1} = 5.6$). Green triangles: quantum confinement only ($V_Y = 0$, $\varepsilon_2 = \varepsilon_{s1} = 22$). (d) Exciton binding energy for organic barriers with $\varepsilon_2 = 3.3$. Blue dots: full calculation with Haken potential (eqn (3)). Purple triangles: full calculation with Bajaj potential (eqn (26)). Stars: experimental data for (PEA)$_2$ (MA)$_{n-1}$Pb$_n$I$_{3n+1}$, from ref. 75.

perovskites. For $n_L \lesssim 3$, the joint effect of dielectric and polaron coupling contributions yields binding energies of the order of several hundreds of meV, much larger than those expected by omitting polaronic short range interaction, and in line with reported experimental and theoretical results.[21,22,26,63]

It is worth noting that the Haken potential is prone to overestimating binding energies, and phenomenological corrections may be needed for more quantitative estimates. One such correction was proposed by Bajaj, who replaced eqn (3) by:[66]

$$V_{eh}^{bulk}(r) = -\frac{q^2}{\varepsilon_s r} - \left(\frac{\varepsilon_\infty}{\varepsilon_s}\right)^\gamma \frac{q^2}{\varepsilon^* r} \frac{e^{-\beta_e r} + e^{-\beta_h r}}{2} \quad (26)$$

where γ was set to 3/5 in order to fit the bulk binding energies of different polar crystals. In Fig. 2(d) we compare E_b calculated with either Haken (blue dots) or Bajaj (purple triangles) potentials. The results are compared with experimental data for Ruddlesden–Popper perovskite of $(PEA)_2$ $(MA)_{n-1}Pb_nI_{3n+1}$, whose effective mass is similar to that of MAPbI$_3$.[75] The dielectric constant of the organic barrier is set to $\varepsilon_2 = 3.3$, as corresponding to PEA (= phenylethylammonium).[26] While the trends and order of magnitude are the same in all cases, the Bajaj potential provides a better match with experiments.

For the physics analysis, however, the Bajaj potential has the handicap of not retrieving the expected limit of $V_{eh}^{bulk} = -q^2/(\varepsilon_\infty r)$ when the inter-particle distance is much smaller than the polaron radius ($r \ll l_i$, with i = e, h). This limitation may be overcome through the use of the Pollman–Büttner potential,[67] which is also claimed to improve quantitative estimates as compared to Haken's in bulk MAPbX$_3$ perovskites.[59] Nonetheless, the Pollman–Büttner potential includes a short range term with various unknown material parameters. Also, in addition to the Coulomb ($1/r$) and Yukawa ($e^{-\beta r}/r$) terms, it contains a non-Yukawa function ($e^{-\beta r}$).[67] This term is likely important in quasi-2D perovskite materials. The electrostatic boundary conditions originating from such a term on the dielectric interface may differ from those presented in this work.

3.2 Self-polarization potential

The exciton properties presented so far are barely affected by the self-polarization potentials. However, a complete description of dielectric confinement requires their inclusion. The weak dielectric screening of the organic barriers enhances not only the e–h Coulomb interaction (V_{eh}), but also the interaction of carriers with their own image charges (V_e^{self} and V_h^{self}). The two effects are known to nearly compensate each other in small crystallites.[77,78] However, in strongly anisotropic systems such as colloidal II–VI nanoplatelets, they have been shown to render sizable global effects on their emission wavelengths or composite properties.[42,69] Further evidence in this direction has been recently obtained in Cs–Pb–Br composites.[79] Below we show that similar effects take place in layered perovskites, and that our image charge method gives a description consistent with atomistic (DFT) simulations.

Fig. 3(a) shows the z-cross section of the self-polarization potential, V^{self}, calculated from eqn (22) for a 2-layer MAPbI$_3$ system surrounded by air or vacuum ($\varepsilon_2 = 1$). The profile of V^{self} is
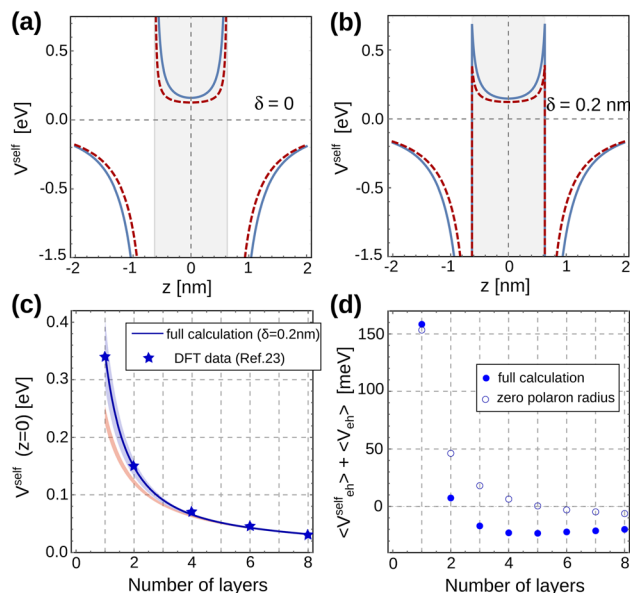

Fig. 3 (a and b) Cross-section of the self-polarization potential along the strong confinement axis of a two-layer MAPbI$_3$ quantum well, with (blue line) and without (red line) the Yukawa correction term. The external medium has $\varepsilon_2 = 1$: (a) the method of shifted-mirror faces is not taken into account ($\delta = 0$); (b) $\delta = 0.2$ nm. (c) Self-polarization potential at the center of the MAPbI$_3$ quantum well structure as a function of the number of layers. Stars: DFT data from ref. 23. Blue line: results obtained for $\delta = 0.2$ nm. Blue-shaded region: results for $\delta = 0$–0.6 nm. Orange-shaded region: same but disregarding V_Y. (d) Sum of the electrostatic interaction energies for the system considered in Fig. 2 as a function of the number of layers in the structure. Full dots (empty circles) include (exclude) V_Y.

similar with (blue line) and without (red line) polaron interactions. For carriers confined within the NPL, V^{self} acts as a repulsive potential, which becomes attractive outside. The effect of polaronic interactions is to provide a moderate increase of the repulsions and attractions (notice the shift between lines).

On the dielectric interfaces, the potential yields non-integrable divergences. This is a well-known limitation of the image charge method when abrupt dielectric interfaces are assumed,[46] arising from the coincident position of carriers and their image charge. Several strategies have been proposed to circumvent this non-physical result.[80–83] All of them rely on the argument that the notion of dielectric constant loses its meaning at distances comparable to the interatomic one, making the abrupt, stepwise dielectric profile model an oversimplification of the dielectric interface.

One strategy to sort this problem is the so-called method of the shifted mirror faces.[68] It consists in introducing a phenomenological parameter δ, physically related to the thickness of a finite-width interfacial layer between adjacent materials. Mathematically, the method simply replaces the $n = \pm 1$ terms in eqn (22) with the following:

$$\frac{q^2 q_{1,C}}{2|2z_i + L_z + \delta|} + \frac{q^2 q_{1,Y} \, e^{-\beta_i|2z_i + L_z + \delta|}}{2|2z_i + L_z + \delta|} + \frac{q^2 q_{-1,C}}{2|2z_i - L_z - \delta|}$$

$$+ \frac{q^2 q_{-1,Y} \, e^{-\beta_i|2z_i - L_z - \delta|}}{2|2z_i - L_z - \delta|}, \quad (27)$$

with δ in the range of a few angstroms. Fig. 3(b) displays the same case as in Fig. 3(a) but employing the method of the shifted mirror faces with $\delta = 0.2$ nm. Now, the self-potential is still discontinuous, yet integrable. It is worth noting that its value influences V^{self} not only at the interfaces, but also throughout all space. Then, the shift parameter δ turns into a fitting parameter – the only one – of this empirical model.

Because quantum confinement sets the peak of the exciton charge density in the $z = 0$ plane of the NPL, the value of the self-polarization potential on this plane is particularly important in determining the exciton energy, and hence the optical band gap. In Fig. 3(c), $V^{self}(z = 0)$ is represented as a function of the number of perovskite layers. The blue-shaded region delimits the results obtained by our model for δ values ranging from 0 to 0.6 nm (upper and lower limits, respectively). For comparison, the results obtained in ref. 23 by means of atomistic (DFT) calculations are also included (blue stars). As can be seen, our model compares very well with the DFT results for a shift parameter of $\delta = 0.2$ nm (blue line in the figure). This agreement not only supports the validity of our model, but it also highlights the need to account for the non-abrupt character of dielectric interfaces (*i.e.* finite δ) in these materials, especially for small n_L, a fact which had been independently pointed out by DFT calculations.[14,46] It is also worth stressing that the agreement with atomistic methods cannot be reached without including short range polaronic (V_Y) effects in the model. To make this point clear, in Fig. 3(c) we also show the self-energy obtained for the same range of δ values, but taking into account V_C contributions only (orange-shaded region).

After integrating eqn (2) on the variational function Ψ_X, the exciton energy can written as:

$$E_X = \langle E_{conf} \rangle + \langle V_{eh}^{self} \rangle + \langle V_{eh} \rangle + E_{gap}^{\Gamma}, \quad (28)$$

where $\langle E_{conf} \rangle$ is the quantum confinement energy, $\langle V_{eh}^{self} \rangle$ the sum of electron and hole self-energy repulsions and $\langle V_{eh} \rangle$ the Coulomb attraction energy. As mentioned before, dielectric confinement enhances both $\langle V_{eh}^{self} \rangle$ and $\langle V_{eh} \rangle$. We study the compensation between the two terms in Fig. 3(d), which is relevant in determining the total exciton energy.

Fig. 3(d) shows the totality of the electrostatic contributions $(\langle V_{eh}^{self} \rangle + \langle V_{eh} \rangle)$, *versus* the number of layers of our MAPbI$_3$ NPL. Full dots (empty circles) are simulations including (excluding) short range terms. In all instances, the lack of compensation between self-energy and Coulomb polarization is evident. As a matter of fact, for thin NPLs ($n_L \lesssim 2$), the energetic destabilization caused by $\langle V_{eh}^{self} \rangle$ is greater than the stabilization caused by $\langle V_{eh} \rangle$, such that the sum becomes positive. This means that thin perovskite layers should experience an electrostatic blueshift in the presence of dielectric confinement, despite the large exciton binding energy. Yukawa corrections do not alter this trend qualitatively.

4 Concluding remarks

We have presented a model to describe exciton states in quasi-2D halide perovskites NPLs. The model can be used to disentangle the roles of quantum confinement (described through effective mass theory), dielectric confinement (image charge method) and polaronic coupling effects (Haken-like potential) in these materials, which facilitates their rational design to achieve desired optoelectronic properties.

We have used the model to study layered MAPbI$_3$ structures. The results show that polaron short range effects become increasingly important as the number of molecular layers in the NPL decreases. This is because quantum and dielectric confinement reduce the exciton radius, making it similar to that of the polaron. It follows that excitons in few-layer structures are largely insensitive to the ionic polarization of the lattice, their response being close to that expected from the high frequency dielectric constant.

All in all, our work paves the way for the use of effective mass based models in the description of exciton properties of metal halide perovskite NPLs. Similar to the case of II–VI nanoplatelets, these can be expected to complement *ab initio* methods with computationally affordable, yet intuitive and reliable descriptions of the optoelectronic properties. Such a possibility can be particularly helpful in the field of hybrid metal halide perovskite nanostructures, where atomistic simulations of excitons become extremely demanding, due to the large unit cells of these materials, the strong spin–orbit interaction (Pb), lack of translational symmetry, varying orientation of organic countercations, and the requirement of accounting for strong e–h correlations (*e.g.* through Bethe–Salpeter method).[26]

Computational codes associated with our model are provided along with this work (ESI†), and can be readily used to investigate excitons in perovskite NPLs built of different materials, by simply providing input bulk effective masses, dielectric constants and LO phonon frequency, which are often found in the literature, along with the dimensions of the structure.

Author contributions

JIC conceived the study. JP and JLM developed the theoretical model (methodology). JLM implemented the computational code (software) and ran the simulations (data curation). All the authors contributed to the analysis and discussion of results, as well as to the writing of the manuscript.

Conflicts of interest

The authors declare no competing financial interests.

Acknowledgements

Notes and references

1 I. C. Smith, E. T. Hoke, D. Solis-Ibarra, M. D. McGehee and H. I. Karunadasa, *Angew. Chem., Int. Ed.*, 2014, **53**, 11232–11235.

2 G. Lanty, K. Jemli, Y. Wei, J. Leymarie, J. Even, J.-S. Lauret and E. Deleporte, *J. Phys. Chem. Lett.*, 2014, **5**, 3958–3963.

3 H. Tsai, W. Nie, J.-C. Blancon, C. C. Stoumpos, R. Asadpour, B. Harutyunyan, A. J. Neukirch, R. Verduzco, J. J. Crochet, S. Tretiak, *et al.*, *Nature*, 2016, **536**, 312–316.

4 T. Hu, M. D. Smith, E. R. Dohner, M.-J. Sher, X. Wu, M. T. Trinh, A. Fisher, J. Corbett, X.-Y. Zhu, H. I. Karunadasa, *et al.*, *J. Phys. Chem. Lett.*, 2016, **7**, 2258–2263.

5 C. Ma, C. Leng, Y. Ji, X. Wei, K. Sun, L. Tang, J. Yang, W. Luo, C. Li, Y. Deng, *et al.*, *Nanoscale*, 2016, **8**, 18309–18314.

6 L. Pedessaau, D. Sapori, B. Traore, R. Robles, H.-H. Fang, M. A. Loi, H. Tsai, W. Nie, J.-C. Blancon, A. Neukirch, *et al.*, *ACS Nano*, 2016, **10**, 9776–9786.

7 J. Liu, Y. Xue, Z. Wang, Z.-Q. Xu, C. Zheng, B. Weber, J. Song, Y. Wang, Y. Lu, Y. Zhang, *et al.*, *ACS Nano*, 2016, **10**, 3536–3542.

8 H. Tsai, W. Nie, J.-C. Blancon, C. C. Stoumpos, C. M. M. Soe, J. Yoo, J. Crochet, S. Tretiak, J. Even, A. Sadhanala, *et al.*, *Adv. Mater.*, 2018, **30**, 1704217.

9 C. M. M. Soe, W. Nie, C. C. Stoumpos, H. Tsai, J.-C. Blancon, F. Liu, J. Even, T. J. Marks, A. D. Mohite and M. G. Kanatzidis, *Adv. Energy Mater.*, 2018, **8**, 1700979.

10 J. Wang, Y. Mi, X. Gao, J. Li, J. Li, S. Lan, C. Fang, H. Shen, X. Wen, R. Chen, *et al.*, *Adv. Opt. Mater.*, 2019, **7**, 1900398.

11 G. Zhou, Y. Xu and Z. Xia, *ACS Appl. Mater. Interfaces*, 2020, **12**, 27386–27393.

12 Y.-T. Li, L. Han, H. Liu, K. Sun, D. Luo, X.-L. Guo, D.-L. Yu and T.-L. Ren, *ACS Appl. Electron. Mater.*, 2022, **4**, 547–567.

13 R. Chakraborty and A. Nag, *J. Phys. Chem. C*, 2020, **124**, 16177–16185.

14 B. Traore, L. Pedessau, L. Assam, X. Che, J.-C. Blancon, H. Tsai, W. Nie, C. C. Stoumpos, M. G. Kanatzidis, S. Tretiak, *et al.*, *ACS Nano*, 2018, **12**, 3321–3332.

15 L. Zhang, X. Zhang and G. Lu, *J. Phys. Chem. Lett.*, 2020, **11**, 6982–6989.

16 J. Yin, P. Maity, R. Naphade, B. Cheng, J.-H. He, O. M. Bakr, J.-L. Brédas and O. F. Mohammed, *ACS Nano*, 2019, **13**, 12621–12629.

17 J. V. Passarelli, C. M. Mauck, S. W. Winslow, C. F. Perkinson, J. C. Bard, H. Sai, K. W. Williams, A. Narayanan, D. J. Fairfield, M. P. Hendricks, *et al.*, *Nat. Chem.*, 2020, **12**, 672–682.

18 S. Tan, N. Zhou, Y. Chen, L. Li, G. Liu, P. Liu, C. Zhu, J. Lu, W. Sun, Q. Chen, *et al.*, *Adv. Energy Mater.*, 2019, **9**, 1803024.

19 J. Even, L. Pedessau and C. Katan, *ChemPhysChem*, 2014, **15**, 3733–3741.

20 M. D. Smith, L. Pedessau, M. Kepenekian, I. C. Smith, C. Katan, J. Even and H. I. Karunadasa, *Chem. Sci.*, 2017, **8**, 1960–1968.

21 J.-C. Blancon, A. V. Stier, H. Tsai, W. Nie, C. C. Stoumpos, B. Traore, L. Pedessau, M. Kepenekian, F. Katsutani, G. Noe, *et al.*, *Nat. Commun.*, 2018, **9**, 2254.

22 K. Tanaka, T. Takahashi, T. Kondo, T. Umebayashi, K. Asai and K. Ema, *Phys. Rev. B: Condens. Matter Mater. Phys.*, 2005, **71**, 045312.

23 D. Sapori, M. Kepenekian, L. Pedessau, C. Katan and J. Even, *Nanoscale*, 2016, **8**, 6369–6378.

24 A. Ghribi, R. Ben Aich, K. Boujdaria, T. Barisien, L. Legrand, M. Chamarro and C. Testelin, *Nanomaterials*, 2021, **11**, 3054.

25 B. J. Bohn, Y. Tong, M. Gramlich, M. L. Lai, M. Döblinger, K. Wang, R. L. Hoye, P. Müller-Buschbaum, S. D. Stranks, A. S. Urban, *et al.*, *Nano Lett.*, 2018, **18**, 5231–5238.

26 R. Chakraborty and A. Nag, *Phys. Chem. Chem. Phys.*, 2021, **23**, 82–93.

27 W. Geng, C.-J. Tong, Y. Zhang and L.-M. Liu, *Adv. Theory Simul.*, 2020, **3**, 2000022.

28 S. Ithurria, M. Tessier, B. Mahler, R. Lobo, B. Dubertret and A. L. Efros, *Nat. Mater.*, 2011, **10**, 936–941.

29 A. W. Achtstein, A. Schliwa, A. Prudnikau, M. Hardzei, M. V. Artemyev, C. Thomsen and U. Woggon, *Nano Lett.*, 2012, **12**, 3151–3157.

30 S. Christodoulou, J. I. Climente, J. Planelles, R. Brescia, M. Prato, B. Martín-García, A. H. Khan and I. Moreels, *Nano Lett.*, 2018, **18**, 6248–6254.

31 R. Benchamekh, N. A. Gippius, J. Even, M. O. Nestoklon, J.-M. Jancu, S. Ithurria, B. Dubertret, A. L. Efros and P. Voisin, *Phys. Rev. B: Condens. Matter Mater. Phys.*, 2014, **89**, 035307.

32 C. Dabard, J. Planelles, H. Po, E. Izquierdo, L. Makke, C. Gréboval, N. Moghaddam, A. Khalili, T. H. Dang, A. Chu, *et al.*, *Chem. Mater.*, 2021, **33**, 9252–9261.

33 F. Rajadell, J. I. Climente and J. Planelles, *Phys. Rev. B*, 2017, **96**, 035307.

34 E. V. Shornikova, D. R. Yakovlev, N. A. Gippius, G. Qiang, B. Dubertret, A. H. Khan, A. Di Giacomo, I. Moreels and M. Bayer, *Nano Lett.*, 2021, **21**, 10525–10531.

35 S. J. Zelewski, K. C. Nawrot, A. Zak, M. Gladysiewicz, M. Nyk and R. Kudrawiec, *J. Phys. Chem. Lett.*, 2019, **10**, 3459–3464.

36 J. Yang and F. Wise, *J. Phys. Chem. C*, 2015, **119**, 26809–26816.

37 S. Ayari, M. T. Quick, N. Owschimikow, S. Christodoulou, G. H. Bertrand, M. Artemyev, I. Moreels, U. Woggon, S. Jaziri and A. W. Achtstein, *Nanoscale*, 2020, **12**, 14448.

38 D. F. Macias-Pinilla, J. Planelles, I. Mora-Seró and J. I. Climente, *J. Phys. Chem. C*, 2021, **125**, 15614–15622.

39 J. Llusar, J. Planelles and J. I. Climente, *J. Phys. Chem. C*, 2019, **123**, 21299–21306.

40 A. H. Khan, G. H. Bertrand, A. Teitelboim, M. C. Sekhar, A. Polovitsyn, R. Brescia, J. Planelles, J. I. Climente, D. Oron and I. Moreels, *ACS Nano*, 2020, **14**, 4206–4215.

41 C. Dabard, V. Guilloux, C. Gréboval, H. Po, L. Makke, N. Fu, X. Z. Xu, M. G. Silly, G. Patriarche, E. Lhuillier, *et al.*, *Nat. Commun.*, 2022, **13**, 5094.

42 A. Polovitsyn, Z. Dang, J. L. Movilla, B. Martín-García, A. H. Khan, G. H. Bertrand, R. Brescia and I. Moreels, *Chem. Mater.*, 2017, **29**, 5671–5680.

43 R. Scott, J. Heckmann, A. V. Prudnikau, A. Antanovich, A. Mikhailov, N. Owschimikow, M. Artemyev, J. I. Climente, U. Woggon, N. B. Grosse, *et al.*, *Nat. Nanotechnol.*, 2017, **12**, 1155–1160.

44 J. Heckmann, R. Scott, A. V. Prudnikau, A. Antanovich, N. Owschimikow, M. Artemyev, J. I. Climente, U. Woggon,

N. B. Grosse and A. W. Achtstein, *Nano Lett.*, 2017, **17**, 6321–6329.

45 J. Planelles, A. W. Achtstein, R. Scott, N. Owschimikow, U. Woggon and J. I. Climente, *ACS Photonics*, 2018, **5**, 3680–3688.

46 C. Katan, N. Mercier and J. Even, *Chem. Rev.*, 2019, **119**, 3140–3192.

47 P. C. Sercel, J. L. Lyons, N. Bernstein and A. L. Efros, *J. Chem. Phys.*, 2019, **151**, 234106.

48 M. Baranowski and P. Plochocka, *Adv. Energy Mater.*, 2020, **10**, 1903659.

49 A. Ferreira, A. Létoublon, S. Paofai, S. Raymond, C. Ecolivet, B. Rufflé, S. Cordier, C. Katan, M. I. Saidaminov, A. A. Zhumekenov, *et al.*, *Phys. Rev. Lett.*, 2018, **121**, 085502.

50 A. Létoublon, S. Paofai, B. Ruffle, P. Bourges, B. Hehlen, T. Michel, C. Ecolivet, O. Durand, S. Cordier, C. Katan, *et al.*, *J. Phys. Chem. Lett.*, 2016, **7**, 3776–3784.

51 M. Sendner, P. K. Nayak, D. A. Egger, S. Beck, C. Müller, B. Epding, W. Kowalsky, L. Kronik, H. J. Snaith, A. Pucci, *et al.*, *Mater. Horiz.*, 2016, **3**, 613–620.

52 A. M. Leguy, A. R. Goñi, J. M. Frost, J. Skelton, F. Brivio, X. Rodríguez-Martínez, O. J. Weber, A. Pallipurath, M. I. Alonso, M. Campoy-Quiles, *et al.*, *Phys. Chem. Chem. Phys.*, 2016, **18**, 27051–27066.

53 I. Anusca, S. Balčiūnas, P. Gemeiner, Š. Svirskas, M. Sanlialp, G. Lackner, C. Fettkenhauer, J. Belovickis, V. Samulionis, M. Ivanov, *et al.*, *Adv. Energy Mater.*, 2017, **7**, 1700600.

54 S. T. A. G. Melissen, F. Labat, P. Sautet and T. Le Bahers, *Phys. Chem. Chem. Phys.*, 2015, **17**, 2199–2209.

55 J. N. Wilson, J. M. Frost, S. K. Wallace and A. Walsh, *APL Mater.*, 2019, **7**, 010901.

56 F. Thouin, D. A. Valverde-Chávez, C. Quarti, D. Cortecchia, I. Bargigia, D. Beljonne, A. Petrozza, C. Silva and A. R. Srimath Kandada, *Nat. Mater.*, 2019, **18**, 349–356.

57 C. Wolf, H. Cho, Y.-H. Kim and T.-W. Lee, *ChemSusChem*, 2017, **10**, 3705–3711.

58 D. Bao, Q. Chang, B. Chen, X. Chen, H. Sun, Y. M. Lam, D. Zhao, J.-X. Zhu and E. E. Chia, *PRX Energy*, 2023, **2**, 013001.

59 E. Menéndez-Proupin, C. L. Beltrán Ríos and P. Wahnón, *Phys. Status Solidi RRL*, 2015, **9**, 559–563.

60 S. A. Bourelle, F. V. Camargo, S. Ghosh, T. Neumann, T. W. van de Goor, R. Shivanna, T. Winkler, G. Cerullo and F. Deschler, *Nat. Commun.*, 2022, **13**, 3320.

61 W. Tao, Q. Zhou and H. Zhu, *Sci. Adv.*, 2020, **6**, eabb7132.

62 S. Neutzner, F. Thouin, D. Cortecchia, A. Petrozza, C. Silva and A. R. S. Kandada, *Phys. Rev. Mater.*, 2018, **2**, 064605.

63 J. A. Sichert, Y. Tong, N. Mutz, M. Vollmer, S. Fischer, K. Z. Milowska, R. García Cortadella, B. Nickel, C. Cardenas-Daw, J. K. Stolarczyk, *et al.*, *Nano Lett.*, 2015, **15**, 6521–6527.

64 L. Zhang, Y. Hao, Y. Wu, W. Qin, X. Liu, B. Cui and S. Xie, *2D Materials*, 2020, **7**, 035020.

65 H. Haken, *Fortschr. Phys.*, 1958, **6**, 271–334.

66 K. Bajaj, *Solid State Commun.*, 1974, **15**, 1221–1224.

67 J. Pollmann and H. Büttner, *Phys. Rev. B: Solid State*, 1977, **16**, 4480.

68 M. Kumagai and T. Takagahara, *Phys. Rev. B: Condens. Matter Mater. Phys.*, 1989, **40**, 12359.

69 J. L. Movilla, J. Planelles and J. I. Climente, *J. Phys. Chem. Lett.*, 2020, **11**, 3294–3300.

70 J. D. Jackson, *Classical Electrodynamics*, John Wiley & Sons, 2021.

71 L.-C. Tu, J. Luo and G. T. Gillies, *Rep. Prog. Phys.*, 2004, **68**, 77.

72 J. Planelles, *Theor. Chem. Acc.*, 2017, **136**, 81.

73 R. F. Stewart, *J. Chem. Phys.*, 1970, **52**, 431–438.

74 E. Menéndez-Proupin, P. Palacios, P. Wahnón and J. Conesa, *Phys. Rev. B: Condens. Matter Mater. Phys.*, 2014, **90**, 045207.

75 M. Dyksik, S. Wang, W. Paritmongkol, D. K. Maude, W. A. Tisdale, M. Baranowski and P. Plochocka, *J. Phys. Chem. Lett.*, 2021, **12**, 1638–1643.

76 V. A. Hintermayr, A. F. Richter, F. Ehrat, M. Döblinger, W. Vanderlinden, J. A. Sichert, Y. Tong, L. Polavarapu, J. Feldmann and A. S. Urban, *Adv. Mater.*, 2016, **28**, 9478–9485.

77 L. E. Brus, *J. Chem. Phys.*, 1983, **79**, 5566–5571.

78 P. Bolcatto and C. Proetto, *Phys. Rev. B: Condens. Matter Mater. Phys.*, 1999, **59**, 12487.

79 S. Caicedo-Dávila, P. Caprioglio, F. Lehmann, S. Levcenco, M. Stolterfoht, D. Neher, L. Kronik and D. Abou-Ras, *Adv. Funct. Mater.*, 2023, 2305240.

80 L. Banyai, P. Gilliot, Y. Hu and S. Koch, *Phys. Rev. B: Condens. Matter Mater. Phys.*, 1992, **45**, 14136.

81 L. Bányai and S. W. Koch, *Semiconductor Quantum Dots*, World Scientific, 1993.

82 P. G. Bolcatto and C. R. Proetto, *J. Phys.: Condens. Matter*, 2001, **13**, 319.

83 J. L. Movilla, J. I. Climente and J. Planelles, *Comput. Phys. Commun.*, 2010, **181**, 92–98.